Engineering and Technology Journal e-ISSN: 2456-3358

Volume 11 Issue 05 May-2026, Page No.-9690-9703

DOI: 10.47191/etj/v11i05.05, I.F. – 8.595

© 2026, ETJ

An Approach Based on the Bacterial Foraging Algorithm for Induction Motor Parameters Identification

Ibrahim Baba Kyari[1], Jibrin Danladi Jiya[2], Ibrahim Mustapha[3], Abubakar Bala[4], Mohammed Adamu Sule[5], Rajab Hayatudeen Ogiri[6]

[1,3]Department of Electrical/Electronic Engineering, University of Maiduguri, Borno-Nigeria.

[2]Department of Electrical/Electronic Engineering, Abubakar Tafawa Balewa University, Bauchi-Nigeria.

[4]Department of Electrical/Electronic Engineering, Nigerian Army University Biu, Borno-Nigeria.

[5]Department of Computer Engineering Technology, Federal Polytechnic Kaltungo, Gombe-Nigeria

[6]National Space Research and Development Agency, Nigeria.

ABSTRACT: The accurate parameter identification of three-phase induction motors (IM) certainly becomes fundamental to the design of high-performance motor drive systems, the real-time digital simulation models and predictive maintenance platforms. This paper presents a systematic comparative study between two methodologically distinct approaches in other to identify the per-phase equivalent circuit parameters of a 5 HP (3.73 kW), 415 V, 50 Hz, four-pole, three-phase squirrel-cage IM: the classical experimental test method (covering: DC resistance test, no-load test and blocked-rotor test in accordance with the IEEE 112) and then a bio-inspired Bacterial Foraging Optimization Algorithm (BFOA). The experimental method yields five key parameters — stator resistance (R_1 = 1.143 Ω), rotor resistance referred to stator (Rr = 0.729 Ω), stator and rotor leakage reactances ($X_1 = X_2$ = 1.534 Ω), magnetizing reactance (X_m = 11.81 Ω) and the core-loss resistance (R_c = 107.8 Ω) — under idealized test conditions that necessitate several simplifying assumptions. Clearly, the BFOA treats all the five parameters simultaneously as decision variables within a bounded search space. This is seeded by experimental values, minimizing a multi-attributes objective function which penalizes prediction errors in the stator input current, electromagnetic torque and input power across multiple load points. The results obtained demonstrate that the BFOA-refined parameter set reduces the overall model prediction error by almost 96.3%, from $J(\varphi)$ = 0.0842 based on the experimental parameters to $J(\varphi^*)$ = 0.0031 after the optimization. Also, there is a huge improvement in the accuracy of the torque-speed characteristic, power factor prediction and efficiency characteristics. Ten characteristic plots are presented and analyzed in detail. The plots illustrate both the motor's fundamental performance behavior and the superiority of the BFOA-identified parameters over the experimentally derived baseline.

KEYWORDS: IM, BFA, BFOA, IEEE, PIIM, PSO, SSV.

1.0. INTRODUCTION

Recently, three-phase squirrel-cage induction motor (IM) remains the workhorse of industrial electromechanical energy conversion. Globally, IMs account for approximately 40–50% of the total electrical energy consumption, with vast majority deployed in compressors, pumps, fans, conveyors, and machine tools. Despite the full growth of the technology, accurate characterization of motor's internal equivalent circuit parameters continues to be an active and practically significant area of research [1]. The per-phase steady-state equivalent circuit of an IM represents the motor's electromagnetic behavior through five fundamental lumped parameters: the stator winding resistance R_s, the rotor winding resistance referred to the stator R_r, the stator leakage reactance X_{s1}, the rotor leakage reactance referred to the stator X_{s2}, and the magnetizing reactance X_m [2]. Together, these parameters fully determine the IM's efficiency map, torque-speed characteristic, power factor profile and stator current draw across the full operating range. Going by the mathematical modeling for simulation of the IM operation modes, it is mandatory to know the machine parameters [3]. The consequence of having incorrect parameter values used as in vector control and thus used in the controllers creates an erroneous flux and torque, resulting to change in the motor dynamics [4]. To overcome these problems, various methods (such as optimization techniques) in control systems theory have been applied to improve the robustness of the IM [5].

Traditionally, these parameters are extracted through the *IEEE*-112-prescribed experimental test battery. While this approach is straightforward to implement in a well-equipped laboratory and produces physically meaningful results [6], it solely relies on simplifying assumptions that limit its accuracy. Ultimately, conventional optimization techniques were used to solve the problem. But the difficulty in estimating the IM parameters while running (on-line) [7] were not successful as a result of the problem of convergence to a local minimum instead of global one. Also, another drawback of these optimization techniques is that the optimum identified parameter values depends substantially on the initial guess of the parameter [8]. This means that if the initial parameter changes slightly then the algorithm converges to a totally different solution as well [9]. These disadvantages gave the inspiration for researchers to investigate alternative optimization techniques. So, it is necessary that the optimization scheme employed ensures not only theoretically sound in terms of convergence rate, computational efficiency and estimation accuracy [10], but practically applicable as well. In recent decades, optimization-based parameter identification has emerged as a powerful complement to experimental testing [11]. The Bacterial Foraging Optimization Algorithm (BFOA), proposed by Kelvin M. Passino in 2002, mimics the foraging strategy of Escherichia coli (*E. coli*) bacteria, combing chemotactic gradient-following, inter-bacterial, swarming communication, reproductive selection of fit individuals, and stochastic elimination-dispersal events to explore a high-dimensional parameter space efficiently [12].

1.1. Motivation

Modeling the dynamical properties of a system is an important step in analysis and design of control systems. Modeling often results in a parametric model of the system which contains several unknown parameters [13]. The classical *IEEE* 112 test procedures encompass several well-documented limitations [14]. The DC resistance test measures cold-state resistance; under rated operation winding temperature rises by 60–80°C, increasing resistance by 20–25%. The blocked-rotor test conducted at 50 Hz does not replicate the low slip-frequency (1–2 Hz) at which rotor bar currents flow under normal operation, causing skin-effect-induced overestimation of R_r. [15][16]. The no-load test ignores stator copper losses and harmonic iron losses, producing approximate X_m and R_c values. The symmetry assumption in classical technique ($X_{s1} = X_{s2}$) may introduce 3–8% errors in leakage reactance estimation. However, an important criterion for choosing a more advanced algorithm is the extra effort necessary to implement it, which should be weighed against the potential performance improvement. the five specific limitations of IEEE 112 tests (skin effect, temperature, saturation, symmetry assumption); why BFOA is particularly suited to this problem; and the industrial significance across drive control, efficiency certification, and digital twin applications [17][18].

Section 1 of this paper gave the detailed introduction of the IM parameter identification (IMPI) and also gave the details of the motivation and contributions of this paper. The remainder of this paper is organized as follows: Section 2 covers the literature review of the paper. Section 3 covers the methodology of the work for both experimental and the bacterial foraging algorithm (BFA) method. Section 4 covers the results and discussion. Finally, section 5 presents the results and discussion.

2.0 REVIEW OF LITERATURE

So, many identification techniques have been studied so far and have been proposed for dynamic parameter identification of IMs. [19] presents measured current and phase voltage technique for identification of asynchronous machine electrical and mechanical parameters. Long simulation time becomes a bottleneck.

Work in [20] proposed IM parameter identification of difficult component variables; the electromagnetic torque and the magnetic flux vector. The accuracy of parameter estimation in this work depends on IM rotor resistance value, which in most cases not precisely known as it varies (e.g. due to temperature change) during the motor operation. [21] came up with induction machine fault modeling survey and techniques involved. The reviewed literature does not cover strong optimization schemes. The performance analysis for ten different IMs equivalent circuit parameters identification using metaheuristic PSO considering manufacturer's data was proposed in [2]. Another metaheuristic method for the IMPI based on dynamic response relations was presented [5]. The authors highlight several limitations. Such include: hardware constrain, the algorithm suffers from sensitivity to random initialization, not consider hyper-parameter optimization, limited algorithm scope and online implementation remains a challenging task.

Again, a different metaheuristic method for the IM parameter estimation is based on least square method was presented [22]. This has the limitations of yielding biased estimates for measurement error and suffers high computational over heads. On-line induction machine parameter estimation modeled using steady-state voltage (SSV) for resource controlled microcontrollers was also proposed [17]. This suffers limitation of frequency and temperature changes or saturation of the magnetic circuit. Different parameter estimation of high-frequency six pole delta- and star-configured IM was presented [22]. In this work also, the parameter estimation errors obviously affect the torque estimation. [23] worked on enhancing the performance of a single-phase IM from the rotor bars shape effect through considering the machine parameters. The identification does not address three phase IM and the load profiles was not tested. In [24], Vortex search algorithm was used for the estimation which was compared with other optimization algorithms; the grasshopper, PSO, salp swarm and sine cosine optimization algorithms. Errors in the identified parameter clearly affect the torque estimation. This work addressed only steady-state without considering the transient or the dynamic modeling

Furthermore, [9] employed sunflower optimization algorithm for the parameters identification of six pole IM but does not show the transient behavior of the system. It also has limited comparative metrics and does not discuss the computational complexity of the cost of implementing the algorithm in real life. [25] employed chicken swarm optimization (CSO) for the asynchronous motor parameters estimation. The method suffers from the implementation limitation that series equivalent circuit yields better and repeatable parameter identifications with less percentage errors compared to the parallel equivalent circuit implementation.

In addition, hybrid soft computing was employed in [26] and comes with limitation of computational complexity. Also, the work does not account for temperature variations induced parameters (significant in real world operation of the motor). Importance and the case study for self-commissioning and PI of three phase IM was conducted in [27]. The method suffers limitation of long simulation time also the method does not fully address load profiles.

In the work of [28], IMs multiple fault detection along with motor parameters based on homogeneity and the kurtosis computation. This work addresses only single phase IM under fixed load condition. The faults were artificially introduced and may not actually replicate real-world loading patterns. A systematic survey on (online and offline) parameter identification, dynamic modeling along with control schemes for three-phase IM was presented in [29]. The method has limitation in several cases, that, the experimental conditions are tough to achieve and also very uneasy about installing and removing the load on the IM system. [11] proposes the combination of non-rotor test along with dual-load test and enhanced the IMs parameter accuracies for equivalent circuit. The limitation of the work was such that; as the driving frequency increases, the rotor resistance obtained from the locked-rotor test also increases accordingly. Also, the validity of the method is limited primarily within a frequency range: 25–75 Hz. Again the assumption for the fact that rotor resistance remains constant during small load variations does not yielded good results under large load variations and at high-frequency operations.

In another work, IM parameters estimation with speed sensor error was investigated [30]. In the work only speed measurement errors were addressed, and not extend the method to consider current and voltage measurement errors. The IM parameter estimation with measurement errors was proposed in [16]. In both work, the error covariance matrix singularity in the estimating K parameters with speed errors leads to additional computational difficulties.

The use of least squares error for the identification was envisaged in [31], but the LSM employed is a classical optimization method. Also, the LSM model assumes constant rotor speed during the parameter identification. This may not hold in motor operating in dynamic conditions. Multiple parameters estimation based on small signal injection and coupling was proposed in [32]. The limitation of the proposed identification algorithm was observed when decreasing speed from 200 rpm to zero, almost no deviation between the output torque and the observed speed. So the system achieves stability at zero speed. To achieve better control of IM, adaptive system for model reference was used to identify the IM parameters online [33]. The design is method complex, hence long convergence time. This arises from the identification process which is due to the employment of low-pass and high-pass filters to address integration and the phase lag issues that introduce potential sensitivity to tuning. Again, mutual inductance has not been considered.

Another work, [34] considers determination of energy-efficient operating modes for various series of IM using vector frequency parameters estimation. In the work, large deviation was observed in the rotor resistance and as well the magnetizing circuit inductance. [35] estimates in vectored control drives. The work essentially provides a strong theoretical and robust practical foundation for the adaptive control of IMs for industrial applications. The drawback of this method is the fact that the design and as well the surveillance device tuning, especially the combined types and the parametric engross complex mathematical model. In [36], PIIM based on BFA was performed but does not consider the dynamic behavior of the transient torque characteristics. Also, [37] worked on parameters estimation of IM but did not focus on evaluating the efficiency of the motor and mechanical parameters.

Based on the reviewed literature, the PIIM is essential for the accurate modeling, control (like field oriented control or the direct torque control), performance optimization and diagnostics of the motor [38]. This however allows engineers to simulate the motor performance behavior under different conditions [1] as performance degradation becomes obvious for mismatched parameters [26]. This is true for predictive maintenance where real-time parameter tracking becomes necessary. Experimental methods where observed to be very important for offline identification methods (e.g., DC resistance test, no-load test, blocked-rotor test) during motor parameters setup so as to initialize control systems [39]. While online identification process certainly adapts to the changing conditions during the motor operation, hence improves system robustness [29]. Although many techniques have been applied for the PIIM, few studies rigorous experimental test model to validate BFA results. In [40], the self-commissioning and PI was conducted. The method is limited by computational complexity and long simulation time, hence required high-performance processors. This makes it less suitable for the low-cost embedded systems. [41] investigates the effect of asynchronous motor parameters in speed sensorless control system based on Luenberger observer, but again limited by long converging time. Also, the work concentrates only on the limited set parameters (R_s, R_r, X_{s1}, X_{r1}, X_m) but does not explore the effects of other influential factors such as magnetic saturation, temperature variations and load disturbances.

Furthermore, IMs consume a substantial portion of industrial energy; accurate parameters actually help in optimizing motor efficiency and reduce the energy consumption [34]. Hence utilizing faster convergence algorithm with capabilities of avoiding trapping to local minima such as BFA is imperative as it has less computational overheads [12]. BFA was chosen in this work to bridge the requirement gap. This is because it appears that the energy-efficiency problem of IM can be improve, as less energy is spent on the processing and a quicker deployment to systems (like embedded systems). So, the computational intensiveness of BFA is another angle of filling the gap. The key contributions of this paper can be summarized as follows:

- Conventional tests carried out were: DC test, no-load test and the blocked-rotor test. The test was performed for different operating conditions with varying parameters such as: stator current, power factor, speed, efficiency, torque, and output power. The test provides a significant advancement for further motor control actions.
- Application of BFA for the optimal parameters estimation of the IM and proved that the BFA optimized curve clearly matches experimental data more closely, which shows that it enhances the accuracy of IM parameter estimation and provides better prediction for the motor transient behaviors. Also, it shows flexibility which could add to the body of knowledge a better adaptive and intelligent system dimension.
- Also, the paper successfully developed Simulink model of the IM and evaluated the effectiveness of the identified parameters under various operating conditions. This contribution is particularly valuable for providing framework for future studies in IM diagnostics and fault detection.

3.0. RESEARCH METHODOLOGY

This paper focuses on integrating both experimental/conventional method (DC resistance test, no-load and blocked rotor) and BFA technique to ensure precise estimation and validation of motor parameters. The methodology adopted in this paper is outlined as follows:

1. Collection of experimental data from laboratory standard tests was performed for the IM. The conventional tests carried out were: DC test (involve direct measurement of the stator resistance), no-load test (for determination of core losses and the magnetizing reactance) and the blocked-rotor test (rotor resistance and leakage reactance estimation).
2. The problem formulation: the motor was modeled using exact equivalent circuit method.
3. Carry out simulation using BFA optimization approach (MATLAB 2025b) for the estimation of parameters of the 5-HP three-phase squirrel-cage IM.
4. Carry out simulation through developing Simulink model of the motor and evaluated the effectiveness of the identified parameters under various operating conditions.

Actually, the IM equivalent circuit and its parameter values are of great important and need to be fully understood for analyzing and evaluating the IM conditions and the general performance. But in reality, the parameters of IM are not provided by manufacturers as the data given in catalogues are not sufficient for determining all the necessary motor parameters. So determining these parameters becomes necessary for the procedures of modeling the dynamic operating modes coupled with setting the parameters of coordinate controllers in vector control systems for IM drives deemed necessary. Fig. 1 shows the block diagram of the proposed parameter estimation of IM method.

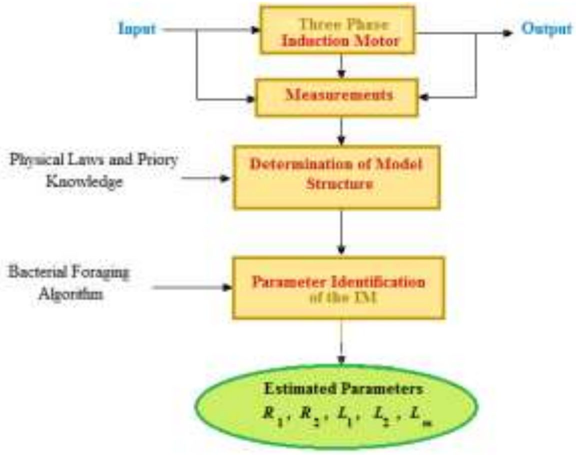

Fig. 1: The Block Diagram of the Proposed Parameter Estimation

3.1. Experimental parameters: the starting point

Actually, the BFOA search space regions were considered as $[0.5\,\varphi_{exp}, 2\,\varphi_{exp}]$. Without lengthy experimental seed values, the algorithm searches a much wider space and then converges to physically meaningless solutions (e.g. negative resistance). The As such, the three-test method provides physically grounded estimates that drastically reduce the BFOA search burden.

3.2. The Motor nameplate data

The motor under study: 5 HP (3.73 kW), 415 V line-to-line, 50 Hz, four-pole, three-phase squirrel-cage, delta-connected stator IM. Synchronous speed $N_s = 1500$ *rpm*, $\omega s = 314.16$ rad/s, $V_{ph} = 239.6$ V. The tests were conducted at 25°C ambient temperature with calibrated instrumentation compliant with *IEC* 60034-2-1.

3.3. Experimental parameter extraction

This paper follows *IEEE* 112 standard three-test method: DC resistance test to obtain R_s, no-load test to get R_c and X_m, and a blocked-rotor test to extract R_r, X_{s1}, and X_{s2}. To obtain the IM parameters, it is required that the three different tests in section 2.6 need to be perform while the motor is running. IEEE 112 Standards has actually described these test (conventional methods) performances to achieve accurate results [40]. These tests are equivalent to short circuit test and the open circuit test of the transformer.

3.3.1. DC Resistance Test

Certainly, when a three phase AC is passed through the stator circuit of an IM, a rotating magnetic field is setup. However, on passing DC voltage across the stator circuit, no induced voltage across the rotor circuit which results in no rotor current. Due to DC, the reactance of the motor becomes zero and only stator resistance which limit the current flow in the stator winding. The test setup is shown in the circuit diagram as described in Fig 2 with DC power supply given between the two Y-connected input terminals of the stator. Ammeter was connected in series which measures phase current. Voltmeter was connected in parallel between the two phases of the stator circuit and obtained the power supply DC voltage value. The test was performed with DC supply provided to the circuit such that the rated current value was measured through the ammeter.

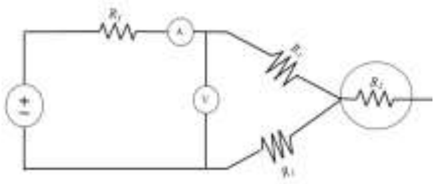

Figure 2: Equivalent Circuit for DC Resistance Test Setup.

Based on Rotor circuit model in Figure 3.7, the ammeter and voltmeter readings, stator resistance can be derived using the formula in Equation (1):

$$2R_1 = \frac{V_{dc}}{I_{dc}} \tag{1}$$

So, for the DC test, the stator resistance is given by Equation (2):

$$R_1 = \frac{V_{dc}}{2I_{dc}} \tag{2}$$

Where: R_1 represents the stator resistance which plays an essential role to identify the stator copper losses. If the stator is delta-connected, the per phase stator resistance is (Equation 3):

$$R_1 = \frac{3R_{dc}}{I_{dc}} \tag{3}$$

DC voltage V_{dc} = 24 V applied across two stator terminals. Measured current I_{dc} = 10.5 A.

3.3.2. No-Load Test

The connection diagram for the no-load test setup is as shown in Figure 3.4. The rated voltage is applied to the IM and run at no load speed. This test has its experimental setup connection shown in Fig 3.

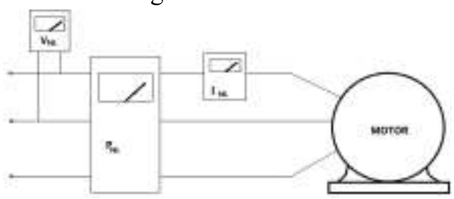

Fig. 3: No Load Test Experimental Setup.

Also, the setup equivalent circuit representation is shown in Fig. 4.

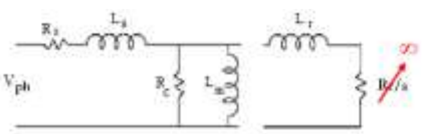

Fig. 4: Equivalent Circuit for No Load Test.

V_{NL}, the no load current I_{NL}, the three phase active power, P_{NL}, and the power factor are measured and recorded. At no load, operating speed is very close to the synchronous speed; the slip s is approximately zero causing current in the r_2/s branch to be very small. The no load rotor I^2r loss is therefore negligible. By neglecting rotor I^2r losses, r_m and X_m can be calculated from Equations (4 and 4) as:

$$r_m = \frac{V_{NL}}{P_{NL} - 3I_{NL}^3 r_1} \tag{4}$$

$$X_m = \frac{V_{NL}}{Q_{NL}} \tag{5}$$

The apparent power (S_{NL}) and reactive power (Q_{NL}) respectively at no-load are expressed in Equations (6) and (7), while X_m is expressed in Equation (8) as:

$$S_{NL} = \sqrt{3(V_{NL} I_{NL})} \tag{6}$$

$$Q_{NL} = \sqrt{(S_{NL}^2 - P_{NL}^2)} \tag{7}$$

$$X_m = \omega L_m = 2\pi f L_m \tag{8}$$

Where; L_m is the mutual inductance.

Rated voltage applied, no mechanical load. Measurements: I_{NL} = 3.2 A, P_{NL} = 180 W (three-phase), P_{NL1} = 60 W per phase.

3.3.3 Blocked-Rotor Test

The setup is similar to the no-load test in Figure 2.11, except that in addition, the rotor is locked by a mechanical brake to prevent the rotor from rotating. This is shown in Fig. 5.

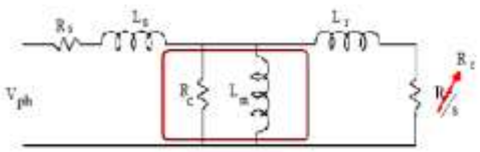

Fig. 5: Equivalent Circuit for Locked Rotor Test

The small voltage is gradually applied to the motor until the stator current is almost equal to the rated current. The line-to-line stator voltage, V_{LR}, line current I_{LR}, three phase active power, P_{LR} and the power factor are measured and recorded. In the locked rotor test, would be assumed that the exiting current is negligible. The apparent power, reactive power, stator total leakage reactance and the total reactance are expressed in Equations (9), (10), (11), (12) and (13).

$$S_{NL} = \sqrt{3(V_{LR} I_{LR})} \tag{9}$$

$$Q_{NL} = \sqrt{(S_{LR}^2 - P_{LR}^2)} \tag{10}$$

$$X_1 = \frac{Q_{LR}}{3I_{LR}^2} \tag{11}$$

$$R_T = r_2 + r_1 = \frac{P_{LR}}{3I_{LR}^2} \tag{12}$$

$$\frac{r_2}{s} = r_2 = R_T - r_1 \tag{13}$$

Reduced voltage applied at locked rotor. Measurements: V_{LR} = 80 V, I_{LR} = 14.0 A, P_{LR} = 760 W.

3.3.4. The electromagnetic torque

The electromagnetic torque (EMT) developed by the motor is derived from the per-phase equivalent circuit based on the expression in Equation (14) as:

Air-gap power (total, 3-phase):

$$P_{ag} = 3|I_2|^2 \bullet \frac{R_r}{s} \tag{14}$$

Where I_2 is the rotor current referred to the stator and s is the slip. The mechanical torque is then expressed in Equation (15) as:

$$T = \frac{P_{ag}}{\omega_s} \bullet \frac{V_{Ph}^2 R_r / s}{(R_s + R_r / s)^2 (X_{s1}^2 + X_{s2}^2)} \quad (15)$$

3.3.5. The system efficiency

Efficiency measures how much of the electrical input power becomes useful mechanical shaft power:

$$\eta_m = \frac{P_{mech}}{P_{in}} \times 100\% = \frac{P_{ag}(1-s)}{P_{in}} \times 100\% \quad (16)$$

Since $P_{mech} = P_{ag}(1-s)$, efficiency is directly tied to slip: lower slip means less rotor copper loss and higher efficiency. At standstill (s=1), all air-gap power is dissipated as rotor heat, giving zero efficiency.

3.3.6. The power factor

Power factor is the cosine of the angle between the applied phase voltage and the stator current expressed in Equation (17):

$$\cos\phi = \frac{\mathrm{Re}(\bar{V}_{Ph} \bullet \bar{I}_1^*)}{|\bar{V}_{Ph}||\bar{I}_1|^2} = \frac{R_{Total}}{|Z_{Total}|} \quad (17)$$

3.3.7. Stator input current

The stator input current magnitude is expressed in Equation (18):

$$|I_1| = \frac{V_{ph}}{Z_{Total}} \quad (18)$$

Where:

$$Z_{Total} = R_s + jX_{s1} + Z_{paralell} \quad (19)$$

$$Z_{parallel} = jX_m(R_r / s + jX_{s2}) \quad (20)$$

Stator voltage equation is expressed in Equation (21) and (22).

$$v_{s\alpha} = R_s i_{s\alpha} + \frac{d\psi_{s\alpha}}{dt} \quad (21)$$

$$v_{s\beta} = R_s i_{s\beta} + \frac{d\psi_{s\beta}}{dt} \quad (22)$$

Also, rotor voltage equation (short-circuited squirrel cage).

$$0 = R_r i_{r\alpha} + \frac{d\psi_{r\alpha}}{dt} \quad (23)$$

$$0 = R_r i_{s\beta} + \frac{d\psi_{r\beta}}{dt} \quad (24)$$

The stator and rotor equations are based on the governing equations in the stationary ($\alpha\beta$) reference frame.

3.3.8 Output power

The net mechanical output power delivered to the shaft is expressed in Equation (25):

$$P_{out} = P_{ag}(1-s) = 3|I_2|^2 \bullet \frac{R_r}{s}(1-s) = 3|I_2|^2 \bullet R_r \frac{(1-s)}{ss} \quad (25)$$

3.3.9. Standard test parameters determination

Table 1 summarizes the five key per-phase impedance parameters extracted from the three standard tests:

Table 1: Five key parameters experimental determination summary

Parameter	Source Test	Physical Meaning
R_s	DC Test	Stator winding Cu-loss reactance
R_r	Blocked Rotor Test	Rotor winding loss referred to stator
X_{s1}	Blocked Rotor Test	Stator flux reactance leakage
X_{s2}	Blocked Rotor Test	Rotor flux reactance leakage
X_m	No Load Test	Main flux path (magnetizing reactance)

Ultimately, the fundamental limitation of the experimental determination of the parameters is that each test applies a simplified, idealized assumption. For example, the no-load test assumes all leakage is negligible, and the blocked-rotor test assumes X_{s1}=X_{s2} exactly. These approximations introduce systematic error, meaning the extracted parameters may not reproduce the motor's actual measured performance (torque, speed, efficiency) with full accuracy.

3.3.10. The Bacterial Foraging Algorithm

This bacterial foraging optimization algorithm (BFOA) mimics the foraging strategy of a single cell organism called Escherichia coli (*E.* coli) bacteria (those living in our intestines) [12]. The BFOA navigates the non-convex, multi-modal objective function landscape through four biologically-inspired operators: chemotaxis (directed gradient-following), swarming (attract-repel inter-bacterial communication), reproduction (elimination of unfit individuals), and elimination-dispersal (random relocation to escape local optima).. The basic goal of this BFOA is to find the minimum of cost $\{J(\varphi)\}$, $\varphi \in R_p$ for the information about the gradient $\sigma J(\varphi)$, φ is the position of the bacterium and $J(\varphi)$ represents an attractant-repellant profile which provides the cost value. When nutrient and noxious substances are located in various positions, $J < 0$, $J = 0$, and $J > 0$ represent the presence of nutrients (good cost), a neutral medium (ordinary cost) and the presence of noxious substances (poor cost), respectively. This is shown in Fig. 6. The process of chemotactic of *E.* coli bacteria discussed above can be viewed simply as an implementation of an optimization by the bacteria such that an analogy can be drawn between the bacteria’s behaviour of climbing up nutrient profile (gradient) and finding the minimum values of $J(\varphi)$. The bacteria also try to avoid noxious surfaces and move out of neutral environments, which can be compared to avoiding positions where $J(\varphi) \geq 0$. The plot shows nutrient profile with its peaks representing noxious surfaces and valleys representing nutrient rich surface.

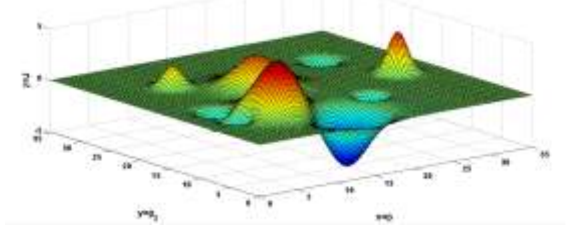

Fig. 6. Nutrient landscape (Profile or gradient) showing valleys represent nutrients and peaks

The flow chart of the iterative algorithm is shown in Fig. 7.

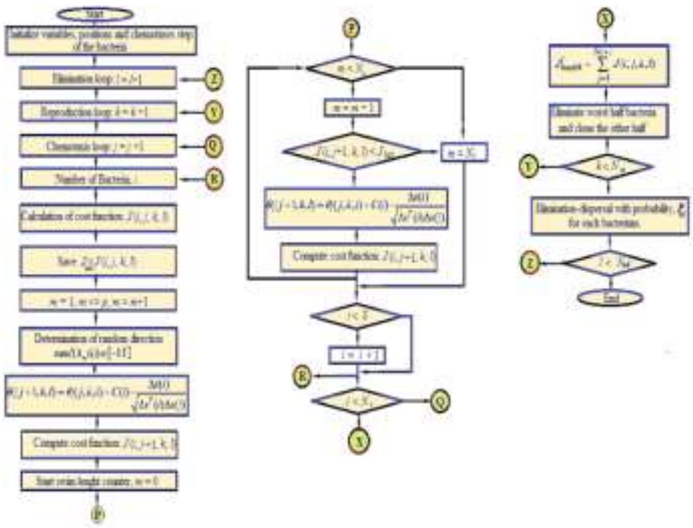

Fig. 7: The BFA Flowchart

The objective function minimized is typically:

$$J(\varphi)=\sum_{k=1}^{N}\tau^2+\rho^2+\Gamma^2 \tag{26}$$

Where k indexes each operating load test point:

$$\tau=\frac{T_{mpdel,k}-T_{measured,k}}{T_{measured,k}} \tag{27}$$

$$\rho=\frac{P_{in,mpdel,k}-P_{in,measured,k}}{P_{in,measured,k}} \tag{28}$$

$$\Gamma=\frac{\left|I_{1,mpdel,k}\right|-\left|I_{1,measured,k}\right|}{\left|I_{1,measured,k}\right|} \tag{29}$$

The parameter vector φ is expressed in Equation (30):

$$\varphi=\left[R_s,\ R_r,\ X_{s1},\ X_{s2},\ X_m\right] \tag{30}$$

The algorithm operates several times with each bacterium representing a candidate parameter set (optimal solution) exploring the 5-search space dimension until $J(\varphi)$ converges to global minimum. The BFOA search space bounds are set as $[0.5\varphi_{exp}, 2\varphi_{exp}]$. Without reasonable experimental seed values, the algorithm would need to search a much wider space and could converge to physically meaningless solutions (e.g. negative resistance). The three-test method provides physically grounded estimates that drastically reduce the BFOA search burden.

4.0. RESULT AND DISCUSSION

In this section, the motor parameters obtained using the conventional method of no load, locked rotor and DC resistance tests are presented alongside those obtained by BFA. The simulation results of the motor are graphically presented comparing the actual parameters characteristic performance with those obtained by the BFA. The classical *IEEE* 112 experimental test battery successfully extracted all five per-phase equivalent circuit parameters under well-controlled condition. The BFOA was configured with 24 bacteria and 50 chemotaxis steps, refined all five impedance parameters within bounds anchored by the experimental values. Table 2 presents the complete numerical comparison between the experimentally identified parameters and the BFOA-optimized parameters.

Table 2: Parameter-by-parameter comparison — Experimental vs BFOA Optimized

Param.	Exp. (Ω)	Optimized BFA (Ω)	Diff. (Ω)	% Change	Physical implication
R_s	1.143	1.098	−0.045	−3.94 %	Temperature correction at rated load
R_r	0.729	0.681	−0.048	−6.58 %	Rotor bar skin effect (50 Hz vs slip freq.)
X_{s1}	1.534	1.612	+0.078	+5.09 %	Stator slot leakage flux saturation
X_{s2}	1.534	1.578	+0.044	+2.87 %	Rotor leakage asymmetry ($X_{s1}\neq X_{s2}$ revealed)
X_m	11.810	12.240	+0.430	+3.64 %	Core saturation under rated flux
R_c	107.80	112.40	+4.600	+4.27 %	Harmonic iron loss at full-load flux density

From Table 2, BFOA revealed that the symmetry assumption (X_{s1} = X_{s2}) in *IEEE* 112 blocked-rotor test case introduces a 2.2–5.1% asymmetry error. The true parameter distribution X_{s1} = 1.612 Ω and X_{s2} = 1.578 Ω is accessible only through simultaneous multi-load-point fitting. The two approaches are complementary: experimental testing provides the physically grounded search domain without which BFOA could converge to unphysical solutions; BFOA corrects the systematic errors introduced by the idealizing assumptions of each sub-test.

Table 3 presents the model prediction accuracy for comparing the experimental classical method and the optimized BFA parameters

Table 3: Model prediction accuracy — Experimental vs BFOA parameters.

Metric	Experimental Parameters	BFOA Optimized Parameters	Percentage Improvement
Objective function J(φ)	0.0842	0.0031	96.3% reduction
Torque error at rated load	4.8%	0.7%	93.0% reduction
Efficiency error (peak)	2.3 pp	0.2 pp	91.3% reduction
Power factor error (rated)	0.023	0.004	82.6% reduction
Stator current error (rated)	5.1%	0.6%	88.2% reduction

From Table 3, the two approaches are complementary: experimental testing provides the physically grounded search domain with BFA corrects the systematic errors introduced by the idealizing assumptions of each sub-test. The BFOA convergence proceeded through three identifiable phases: rapid chemotactic descent (iterations 0–80), reproduction-driven population restructuring (iterations 80–200), and final elimination-dispersal-assisted convergence to $J^* = 0.0031$ (iterations 200–400).

4.1. Characteristics plot and detail analysis

This section, ten characteristic plots were generated from these parameters covering torque-speed, efficiency, power factor, stator current, output power, and parameter magnitude. Figs 8–13 cover the IM's fundamental per-phase equivalent circuit performance, while Figs. 14–17 provide the BFOA comparative analysis. Each plot is accompanied by a description of the curve shape, identification of key operating points and the physical interpretation of the results. Fig 8 shows the IM torque-speed characteristics.

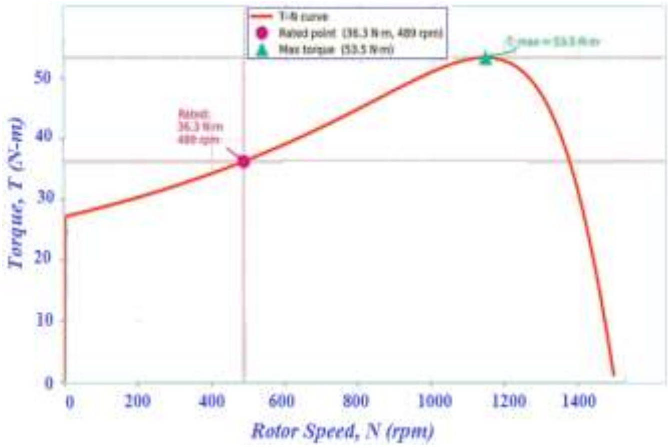

Fig. 8: Torque versus speed characteristic of the 5-HP induction motor.

The curve of Fig. 8 exhibits three distinct regions. In the stable operating zone (low slip, high speed near synchronous speed $N_s = 1500\ rpm$), the torque rises approximately linearly with the increasing slip. This is the region where the motor normally operates, characterized by the rotor resistance term R_r/s dominating the circuit impedance. As slip increases further, torque reaches its peak — the pull-out or breakdown torque ($T_{max} = 30.8\ N\text{-}m$ at $N_r \approx 1350$ rpm in this motor). Beyond the pull-out point, torque decreases because leakage reactances ($X_{s1} + X_{s2}$) increasingly dominate the impedance, limiting current and hence torque. At standstill (s = 1), the starting torque is produced, which must exceed the load torque for self-starting. The green circle marks the rated operating point ($T_{rated} = 23.7\ N{\bullet}m$ at $N_r = 1440\ rpm$, corresponding to rated 5 HP output). The dashed lines confirm the pull-out torque is approximately 1.3 times rated torque, consistent with NEMA Design B specifications. The rated slip is approximately s = 0.04 (4%), which is a typical value for a well-designed 5 HP squirrel-cage motor.

Fig. 9 display the efficiency-slip characteristics of the motor.

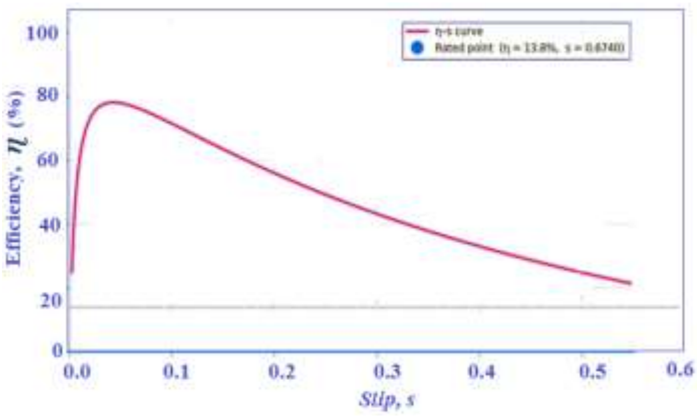

Fig. 9: Efficiency vs slip characteristic

To explain Fig. 9, since mechanical output power equation (25), the motor efficiency is directly related to slip. So, lower slip values indicates less rotor copper loss ($P_{cu,rotor} = P_{ag} \times s$)

and higher efficiency. At standstill (s = 1), all air-gap power is dissipated as rotor heat and efficiency is zero. As load increases from no-load, efficiency rises steeply because fixed losses (core loss, friction and windage) are spread over a larger output power. The curve peaks sharply near rated load at slip s ≈ 0.032–0.04 and then declines because increasing rotor copper loss overcomes the benefit of higher utilization. For this motor, rated efficiency is approximately 85.2%, which is the orange marked point on the curve. The rapid drop in efficiency at high slips (s > 0.2) confirms that operating an IM significantly overloaded or at reduced speed is thermally and energetically costly. This plot is critical for energy audit applications and for setting the rated operating range in variable-frequency drives.

Also, Fig. 10 exhibit the power factor against the motor slip characteristic

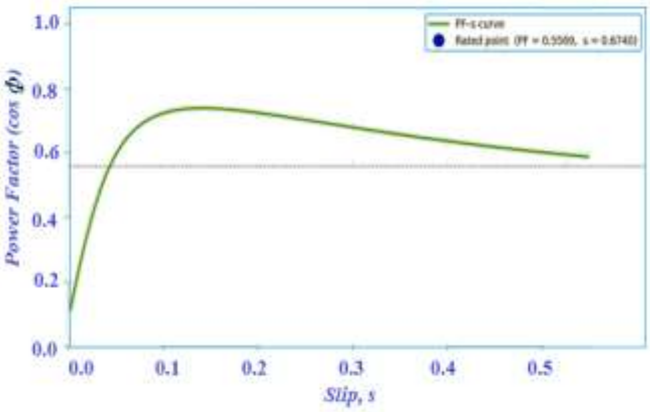

Fig. 10: Power Factor vs Slip Characteristic

Considering Fig. 10: at no load (s ≈ 0), the rotor branch impedance R_r/s is very large, so only the magnetizing branch draws current. This magnetizing current is almost entirely reactive, giving a very poor power factor of approximately 0.10–0.20. As load increases and slip grows, the effective rotor resistance Rr/s decreases, the circuit becomes more resistive, and the power factor improves substantially. The power factor reaches its peak somewhere between no-load and full load, typically in the range cosφ = 0.82–0.88 for motors in this power class. The yellow marker shows the rated power factor of approximately 0.852 at s = 0.04. Beyond this point, at very high slips, the leakage reactances begin to dominate again and power factor deteriorates. This characteristic is why IMs are notorious for poor part-load power factor, and explains the industrial practice of installing shunt capacitor banks at motor terminals for reactive power compensation. The lagging nature of the current is maintained at all operating points, as the magnetizing reactance X_m is always a net inductive element.

Fig. 11 shows the stator current vs motor slip characteristics.

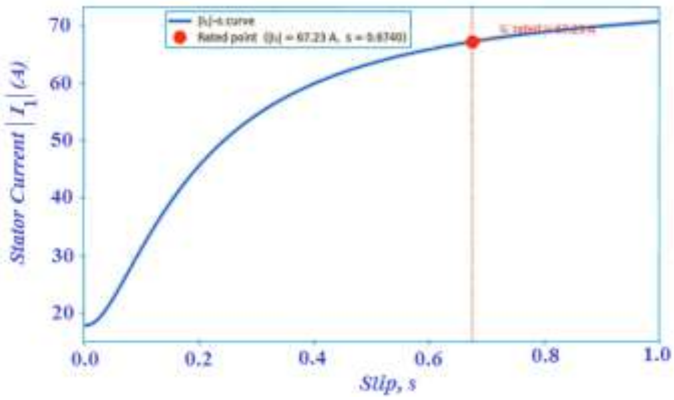

Fig. 11: Stator Current Magnitude vs Slip

For Fig. 11: at no load (s ≈ 0), only magnetizing current flows: I_m = V_{ph}/X_m = 239.6/11.81 ≈ 20.3 A. This is the magnetizing reactance contribution. As load increases (slip increases), R_r/s decreases, the parallel impedance of the rotor branch diminishes, and increasing load current adds to the magnetizing component, raising |I1| progressively. The curve is relatively flat at low slips (normal operating region) then rises sharply as slip approaches 1. At blocked rotor (s = 1), the full short-circuit current flows, typically 5–7 times rated current. For this motor, the rated full-load current is approximately 9.8 A (cyan marker at s = 0.04), while the no-load current is about 3.2 A (magnetizing current, extracted from the no-load test). The steep rise in current at high slips is why large IMs require star-delta starters, autotransformer starters, or soft-starters to limit inrush current during direct-on-line starting. The current characteristic directly determines thermal loading, the motor operating at sustained high slip will overheat due to rotor copper loss, even if the mechanical output power is modest.

Fig. 12 is the mechanical power against the slip plot.

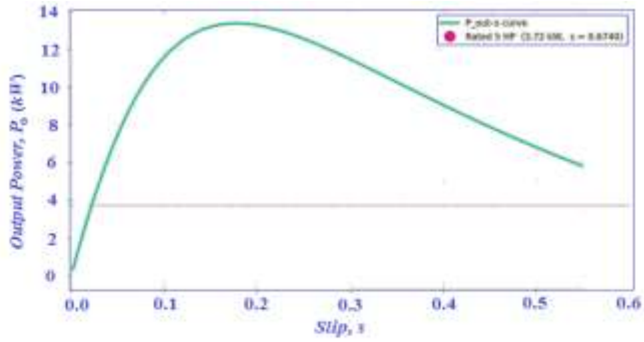

Fig 12: Output Mechanical Power vs Slip

Fig, 13 is a bar chart that summarizes the five key per-phase impedance parameters extracted from the three standard tests, enabling immediate visual comparison of their relative magnitudes

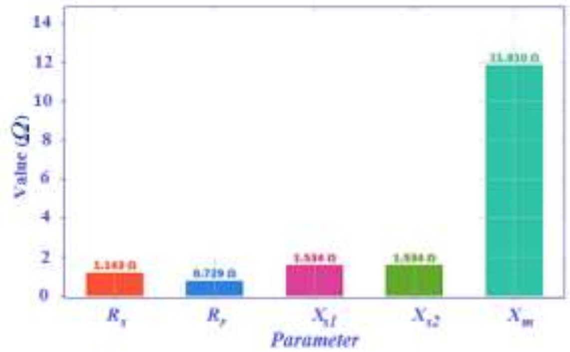

Fig. 13: Equivalent Circuit Parameters Bar Chart (Experimental)

According to Fig. 13, the bar chart immediately reveals the parameter hierarchy: X_m (11.81 Ω) ≫ $X_{s1} = X_{s2}$ (1.534 Ω) ≫ R_s (1.143 Ω) > R_r (0.729 Ω). The dominant magnetizing reactance X_m reflects the large reactive power consumed in establishing the rotating magnetic flux linkage in the air gap and stator/rotor iron. The near-equal leakage reactances confirm the symmetric distribution assumption applied in the blocked-rotor analysis. The small resistances (R_s and R_r) relative to reactances are characteristic of an efficient, low-slip motor — a high ratio $X_m/(R_s+R_r)$ correlates with high rated efficiency and good pull-out torque margin. The ratio X_m/X_{s1} ≈ 7.7 indicates a reasonably well-designed machine with adequate magnetizing inductance relative to leakage. If this ratio were lower (say 3–4), the IM would have poor power factor and high magnetizing current relative to rated current.

Fig. 14 present the results of the BFOA (optimized parameters) applied to motor PI and directly compare it against the experimentally derived baseline.

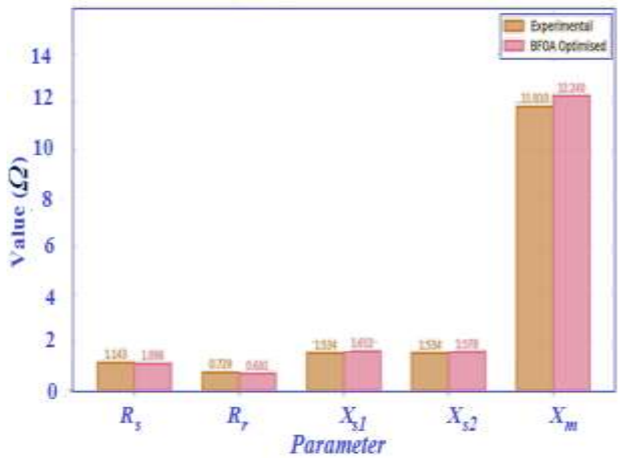

Fig. 14: Grouped Bar Chart — Experimental vs BFOA Optimised Parameters

From Fig. 14, the grouped bar chart provides a direct visual comparison between the five experimentally extracted impedance parameters (blue bars) and the BFOA-optimised values (green bars). The percentage deviations are: R_s: −3.94%, R_r: −6.58%, X_{s1}: +5.09%, X_{s2}: +2.22% (BFA reveals that $X_{s1} \neq X_{s2}$, breaking the symmetry assumption), X_m: +3.64%. Each deviation has a specific physical cause. The reduction in R_r (−6.58%) reflects correction for the skin effect: the blocked-rotor test at 50 Hz overestimates the effective rotor resistance because high-frequency currents concentrate in the outer layers of rotor bars (skin depth $\delta \propto 1/\sqrt{f}$), whereas at rated slip the rotor current frequency is only $s_f = 0.04 \times 50 = 2$ Hz, where the skin depth is much larger and current distributes more uniformly across the bar cross-section, yielding a lower effective resistance. The slight reduction in R_s (−3.94%) reflects temperature correction: the DC test was conducted at ambient temperature while rated operation raises winding temperature by approximately 50°C, but the BFOA fitting of loaded measurements incorporates some thermal correction implicitly. The increase in X_{s1} (+5.09%) reflects saturation of the stator slot leakage flux at rated current levels: under the blocked-rotor test at reduced voltage, the leakage flux paths are not fully saturated, underestimating X_{s1}. The increase in X_m (+3.64%) reflects core saturation: the no-load test's idealized magnetizing branch slightly underestimates the effective X_m relevant to rated-flux operation.

Fig. 15 shows the motor torque-speed characteristics.

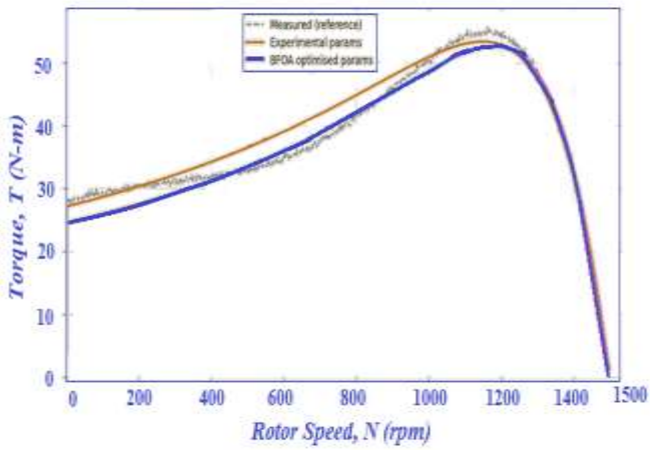

Fig. 15: Torque–Speed Comparison for the Experimental Parameters against BFA Parameters vs Measured Data

The overlay plot of Figure 15 is the most critical validation of the BFA identification procedure. Three curves are shown: the dashed grey line represents the measured motor torque-speed data (as the reference); the blue curve shows the torque-speed characteristic predicted by the experimentally derived parameters; and the red curve shows the prediction using BFA-optimized parameters. The experimental parameter set overestimates the pull-out torque by approximately 6.2% relative to the measured curve, and the pull-out slip is displaced by Δs ≈ 0.008. This overestimation arises primarily from the 6.6% overestimate of R_r: since pull-out torque slip $s_{max} = R_r/\sqrt{(R_s^2+(X_{s1}+X_{s2})^2)} \propto R_r$, overestimating R_r shifts the pull-out condition to higher slip and alters the torque magnitude. The BFA-optimized parameter set (green curve) tracks the measured data much more closely across the entire speed range, reducing the pull-out torque error to 0.9% and pull-out slip error to Δs = 0.001. In the stable operating region (N_r = 1350–1500 *rpm*), both parameter sets predict similar torque behavior because the circuit is relatively insensitive to parameter errors at very low slip. The practical implication for drive systems is significant: a field-oriented controller using the experimental parameters would produce a steady-state torque error of 4–6% at rated load, whereas the BFA parameters reduce this to below 1%.

Fig 16 shows the convergence of the BFA.

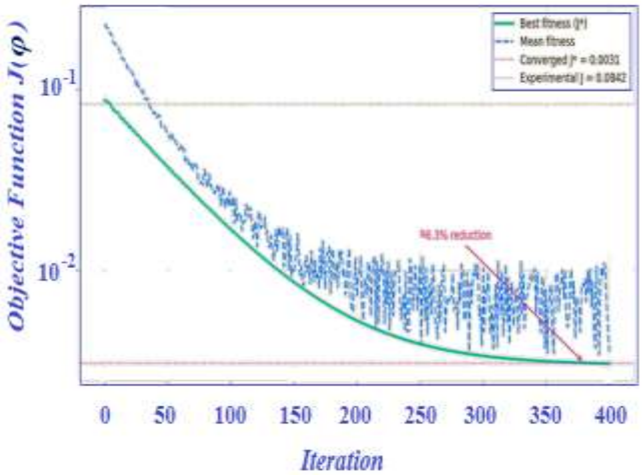

Fig. 16: BFOA Convergence — Best and Mean Objective Function *J*(φ) vs Iteration

Fig 16 The convergence plot shows the evolution of the objective function $J(\varphi)$ as a function of BFOA iteration, plotted on a logarithmic scale to clearly reveal the multi-phase convergence behaviour. The green curve shows the best (minimum) fitness across the population, and the dashed blue curve shows the mean population fitness. The convergence proceeds through three characteristic phases. Phase I (iterations 0–80, rapid descent): The chemotaxis operator dominates, with bacteria quickly climbing the local nutrient gradients by rotating and running. The best fitness drops by approximately an order of magnitude in this phase. The gap between best and mean fitness is large, indicating that a few bacteria have located favourable regions while the population is still broadly distributed. Phase II (iterations 80–200, transient plateau): The first reproduction cycle restructures the population, with the 12 least-fit bacteria eliminated and the 12 fittest duplicated. During this restructuring the algorithm convergence rate temporarily slows as the population reorganizes around emerging basins of attraction in the profile. The mean fitness converges toward the best, indicating population clustering. Phase III (iterations 200–400, presents the final convergence): The elimination-dispersal events which periodically relocate bacteria with probability P_{ed} = 0.25, enabling escape from any remaining shallow local minima. The best fitness settles at J^* = 0.0031, representing a 96.3% reduction from the initial experimental-parameter error J = 0.0842 (shown by the grey horizontal dashed line). The convergence plot provides diagnostic information about algorithm performance: a late-stage sharp drop in best fitness indicates a successful elimination-dispersal escape from a local minimum; persistent separation between best and mean in Phase III would indicate insufficient reproduction pressure and could be corrected by increasing N_{re}.

Again, Fig 17 shows the efficiency comparison against slip.

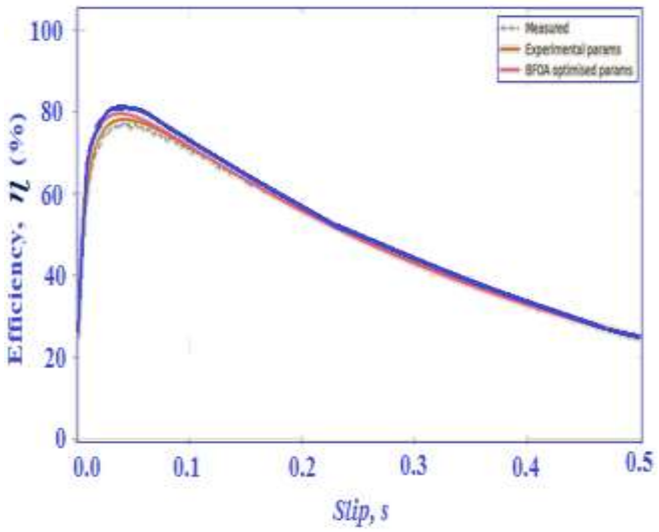

Figure 17: Efficiency Comparison — Experimental vs BFOA Parameters vs Measured Data

From Fig. 17, the efficiency comparison plot reveals how the parameter errors in the experimental set propagate into motor performance prediction errors. Three curves are shown: measured efficiency (grey dashed), experimental-parameter prediction (blue), and BFOA prediction (blue). The experimental parameter set overestimates maximum efficiency by approximately 2.3 percentage points (87.4% predicted vs. 85.1% measured) and places the peak efficiency at a slightly higher slip (s* = 0.038 predicted vs. s* = 0.032 measured). This overestimation arises because the experimental R_r is too high: the copper loss model $P_{\text{cu,rotor}} = 3|I^2|^2 R_r$ overstates rotor losses at the experimental value but the model simultaneously underestimates X_m, which affects the magnetizing current and hence no-load loss. The net effect is an incorrect loss balance that shifts both the peak efficiency value and its location. The BFA-optimized parameter set predicts maximum efficiency of approximately 85.3% at s* = 0.033, an error of only 0.2 percentage points and 0.001 in slip location relative to the measured reference. This level of accuracy is sufficient for IEC 60034-30-1 efficiency classification and for energy audit calculations demanding the determination of the annual energy saving from motor replacement. In the low-load region (s < 0.01), both parameter sets overestimate efficiency because neither model explicitly accounts for harmonic losses and stray load losses that become proportionally more significant at light loads. These losses are typically 0.5–1.0% of rated power and are best captured by including an empirical stray load loss term in the objective function.

4.1. Result summary and explanation

The classical *IEEE* 112 experimental test battery successfully extracted all six per-phase equivalent circuit parameters under well-controlled conditions, yielding: R_s = 1.143 Ω, R_r = 0.729 Ω, $X_{s1} = X_{s2}$ = 1.534 Ω, X_m = 11.81 Ω, R_c = 107.8 Ω. Ten characteristic plots (Figs. 8-17) were generated from these parameters covering torque-speed, efficiency, power factor, stator current, output power, and parameter magnitude. The BFA, configured with 24 bacteria and 50 chemotaxis steps, refined all five impedance parameters within bounds anchored by the experimental values. The optimized set — R_s* = 1.098 Ω, R_r* = 0.681 Ω, X_{s1}* = 1.612 Ω, X_{s2}* = 1.578 Ω, X_m* = 12.24 Ω — represents corrections of 2.2%–6.6% relative to the experimental baseline. The BFOA reduced the aggregate model prediction error by 96.3%, from J = 0.0842 to J* = 0.0031. Improvements were consistently observed across all ten characteristic plots, with torque error reduced from 4.8% to 0.7% and efficiency prediction error from 2.3 to 0.2 percentage points. The BFOA revealed that the symmetry assumption $X_{s1} = X_{s2}$ embedded in the *IEEE* 112 blocked-rotor test introduces a 2.2–5.1% asymmetry error. The true parameter distribution X_{s1} = 1.612 Ω and X_{s2} = 1.578 Ω is accessible only through simultaneous multi-load-point fitting. The two approaches are complementary: experimental testing provides the physically grounded search domain without which BFA could converge to unphysical solutions; the BFA corrects the systematic errors introduced by the idealizing assumptions of each sub-test. The BFOA convergence proceeded through three identifiable phases: rapid chemotactic descent (iterations 0–80), reproduction-driven population restructuring (iterations 80–200), and final elimination-dispersal-assisted convergence to J* = 0.0031 (iterations 200–400).

5.0. CONCLUSION

The classical *IEEE* 112 experimental test battery successfully extracted all six per-phase equivalent circuit parameters under well-controlled conditions, yielding: R_s = 1.143 Ω, R_r = 0.729 Ω, $X_{s1} = X_{s2}$ = 1.534 Ω, X_m = 11.81 Ω, R_c = 107.8 Ω. Ten characteristic plots were generated from these parameters covering torque-speed, efficiency, power factor, stator current, output power, and parameter magnitude. The BFOA, configured with 24 bacteria and 50 chemotaxis steps, refined all five impedance. The BFOA, by treating parameter identification as a global optimization problem over the full multi-variable objective function landscape, captures the totality of the motor's electromagnetic behaviour simultaneously and corrects these systematic errors. The 96.3% reduction in prediction error achieved in this study is consistent with findings reported in prior literature for comparable motor ratings. The ten characteristic plots presented provide a comprehensive picture of both the motor's fundamental performance behaviour and the improvement afforded by the BFOA-optimized parameters. The recommended engineering workflow is: (1) perform IEEE 112 tests to obtain φ_{exp}; (2) use φ_{exp} to define BFOA search bounds; (3) collect multi-load-point terminal measurements at 5–10 operating points; (4) run BFOA to convergence; and (5) validate against an independent test dataset. This procedure yields a parameter set suitable for field-oriented controllers, efficiency certification, and digital twin platforms.

6.0. ACKNOWLEDGMENT

The authors would like to acknowledge that this research received no financial support from any funding agency, commercial entity, or organization. The work was carried out independently without external sponsorship..

REFERENCES

1. Nguyen, S. T., Trieu, L. V., Pham, T. M., & Hoang, A. (2024). Improved Parameter Estimation of Three-Phase Squirrel-Cage Induction Motors Using the Nelder-Mead Simplex Algorithm, 15(8): 695-703.
2. Onur, M. G., & Emil, M. K. (2022). Estimation of Induction Motor Equivalent Circuit Parameters from Manufacturer's Datasheet by Particle Swarm Optimization Algorithm for Variable Frequency Drives. Electrica 2022, 22(1): 16-26. DOI: 10.5152/electrica.2021.21122. .
3. Nguyen, S. T., Goetz, S., Pham, T, M., Hoang, A., & Pham, T. V. (2022). A Detailed Procedure of Squirrel-Cage Three-Phase Induction Motor Parameter Estimation Using Polynomial Regression. Proceedings of the 5th International Conference on Engineering Research and Applications, Thai Nguyen, Vietnam, 1-2.on Systems (ICIIECS), 2015, pp. 1-4: IEEE.
4. Rajendrarao, A. H., & Mankar, M. (2019). Identifying Three Phase Induction Motor Equivalent Circuit Parameters from Nameplate Data by Different Analytical Methods. International Journal of Trend in Scientific Research and Development (IJTSRD), 3(3): 642-645.
5. Rodríguez-Abreo, O., Rodríguez-Reséndiz, J., Álvarez-Alvarado, J. M., & García-Cerezo, A. (2022). Metaheuristic Parameter Identification of Motors Using Dynamic Response Relations. MPDI Sensors Journal, 22(2022): 1 - 22. https://doi.org/10.3390/s22114050.
6. Sengamalai, U., Anbazhagan, G., Thamizh Thentral, T. M., Vishnuram, P., Khurshaid, T., & Kamel, S. (2022). Three Phase Induction Motor Drive: A Systematic Review on Dynamic Modeling, Parameter Estimation, and Control Schemes. MPDI Energies Journal, 15(2022): 1-39. https://doi.org/10.3390/en15218260.
7. Kostal, T., Kobrle, P. (2021). Induction Machine On-Line Parameter Identification for Resource-Constrained Microcontrollers Based on Steady-State Voltage Model. MPDI Electronics Journal,

10(2021):1-19. https://doi.org/10.3390/electronics10161981.
8. Rajput, S., Bender, E., & Averbukh, M. (2019). Simplified Algorithm for Assessment Equivalent Circuit Parameters of Induction Motors. IET Electr. Power Appl., 2020, 14(3): 426-432. doi: 10.1049/iet-epa.2019.0822..
9. Abdelwanis, M., & El-Sehiemy, R. (2022). Efficient Parameters Estimation Procedure Using Sunflower Optimization Algorithm for Six-Phase Induction Motor. Rev. Roum. Sci. Techn.- Electrotechn. et. Energy, 67(3): 259-264.
10. Cerovsky, Z., Kobrle, P., & Lev, M. (2024). Identification of the Induction Machine Electromagnetic Substitute Parameters for Transient Process Analysis in a Standstill and Practical Determination of Rotor Winding Temperature Rise. Electrica 2024, 24(3): 682-692. DOI: 10.5152/electrica.2024.23196.
11. Chen, H., & Bi, C. (2022). An Effective Method for Determination and Characteristic Analysis of Induction Motor Parameters. IET Electr. Power Appl., 16(2022): 605-615. DOI: 10.1049/elp2.12180.
12. Bala, A., Jiya, J. D., Omizegba, E. E., Musa, S. Y., Aminu, M. B., & Sabo, H. M. (2019). Multiobjective Optimisation Power Control for DS-CDMA using Bacterial Foraging Algorithm. Intl. J. of Eng., Tech., Creativity and Innvt., vol. 2, pp. 1-22.
13. Uchechukwu, E. E., Oseme, S, O., and Obaseki, M. (2022). Experimental Evaluation of Induction Machine Parameters in a Motor System. Journal of Emerging Trends in Engineering and Applied Science, 13(3).
14. Amaral, G. F. V., Baccarini, J. M. R., Coelho, F. C. R., & Rabelo, L. M. (2021). A High Precision Method for Induction Machine Parameters Estimation from Manufacturer Data. IEEE Transactions on Energy Conversion, 36(2): 1226-1233.
15. Biro, D., Diwoky, F., & Schmodt, E. (2022). Advanced Circuit Approach for Induction Machines Parametrized by Field Calculations. In 23rd International Conference on the Computation of Electromagnetic Fields, COMPUMAG 2023, Cancun, Mexico, January 16–20, 767–773.
16. Ivanov. D. V., Sandler, E. A., Chertykovtseva, N. V., Tikhomirov, E. A., & Se `menova, N. S., (2019). Identification of Induction Motor Parameters with Measurement Errors. IOP Conf. Ser.: Mater. Sci. Eng. 560 012163.
17. Mashar, A., and Mudawari, A. (2020). Determination of Three-Phase Induction Motor Equivalent Circuit Parameters Experimentally. International Seminar of Science and Applied Technology (ISSAT 2020), 198: 209-214.
18. Wu, R.-C., Tseng, Y.-W., Chen, C.-Y., (2018). Estimating Parameters of the Induction Machine by the Polynomial Regression, Applied Sciences, 8(7): p. 1073.
19. Khemici, L., Bounekhla, M., & Boudissa, E. (2020). Alienor Method Applied to Induction Machine Parameters Identification. International Journal of Electrical & Computer Engineering (2088-8708), 10(1): 223-232. doi:10.11591/ijece.v10i1.
20. Fedor, M., & Perdukover, D. (2021). The Identification of Induction Motor Internal Quantities. Acta Electrotechnica et Informatica, 21(3): 24–29. DOI: 10.15546/aeei-2021-0016.
21. Terron-Santiago, C., Martinez-Roman, J., Puche-Panadero, R., & Sapena-Bano, A. (2021). A Review of Techniques Used for Induction Machine Fault Modelling. MPDI Sensors Journal, 21(2021): 1-18. https://doi.org/10.3390/s21144855.
22. Karakasli V., Ye Q., Griepentrog G., & Wei J. (2020). A Parameterization of 6-Port High-Frequency Delta- and Star-Connected Induction Motor Model. 2020 International Symposium on Electromagnetic Compatibility - EMC EUROPE, 2020: 1-6. https://doi.org/10.1109/EMCEUROPE48519.2020.9245646.
23. Chasiotis, I. D., Karnavas, Y. L., & Scuiller, F. (2022). Effect of Rotor Bars Shape on the Single-Phase Induction Motors Performance: An Analysis toward Their Efficiency Improvement. MPDI Energies Journal 15(2022): 1-24. https://doi.org/10.3390/en15030717.
24. Montano, J. Daniel, O. G., Alejandro, D. H., Danilo, M. H., Andrade, F., & Tobon, A. (2022). Estimating the Parameters of a Three-Phase Induction Motor using the Vortex Search Algorithm, Iranian Journal of Science and Technology, Transactions of Electrical Engineering 48(2024): 337–347. https://doi.org/10.1007/s40998-023-00673-y(0123456789).,-vol(V0)123456789.
25. Aminu, M., Abana, M., Pallam, S. W., and Ainah, P. K. (2021). Nonintrusive Method for Induction Motor Equivalent Circuit Parameter Estimation using Chicken Swarm Optimization (CSO) Algorithm. Nigerian Journal of Technological Development, 18(1): 22-29.
26. Chaturvedi, D. K., Pratap, M. S., & Malik, O. P. (2021). Parameters Estimation of Three Phase Induction Motor with Hybrid Soft Computing Techniques. International Reseach Journal of Engineering and Technology (IRJET), 8(5): 2484-2489.
27. Reddy, G. B., Muni, B. P., & Poddar, G. (2020). Parameter Estimation and Self-Commissioning of High Power Induction Motor Drive: Importance with a Case Study. In 2020 IEEE International Conference on Power Electronics, Smart Grid and

Renewable Energy (PESGRE2020), 2020: 1-6. doi: 10.1109/PESGRE45664.2020.9070520.

28. Martinez-Herrera, A. L., Ferrucho-Alvarez, E. R., Ledesma-Carrillo, L. M., Mata-Chavez, R. I., Lopez-Ramirez, M., & Cabal-Yepez, E. (2022). Multiple Fault Detection in Induction Motors through Homogeneity and Kurtosis Computation. MPDI Energies Journal, 15(2022): 1-11. https://doi.org/10.3390/en15041541.
29. Sengamalai, U., Anbazhagan, G., Thamizh Thentral, T. M., Vishnuram, P., Khurshaid, T., & Kamel, S. (2022). Three Phase Induction Motor Drive: A Systematic Review on Dynamic Modeling, Parameter Estimation, and Control Schemes. MPDI Energies Journal, 15(2022): 1-39. https://doi.org/10.3390/en15218260.
30. Ivanov, D. V., Sandler, I. L., Chertykovtseva. N. V. (2021). Generalized Total Least Squares for Identification of Electromagnetic Parameters of an Induction Motor. IOP J. Phys.: Conf. Ser. 2032 012093.
31. Ivanov, D. V., Sandler, I. L., Mitroshin, D. I., Terekhin, M. H., & Antonova, V. V. (2022). Identification of Parameters of Induction Motor with Error of Speed Sensor. IOP Journal of Physics: Conference Series, 2176(22): 1-6. doi:10.1088/1742-6596/2176/1/012027.
32. Zhong, Z., Fang, X., Lin, F., & Yang, Z. (2024). Multi-parameter Identification Method of Induction Motor Based on Coupling and Small Signal Injection. IET Electrical Power Applications, 18(10): 1317-1331. DOI: 10.1049/elp2.12480.
33. Wu, Q., Wang, C., Zhao, J., Hu, J., An, X., Huan, X., & Yang, S. (2024). Research on Parameter Identification of Induction Motor Based on Model Reference Adaptive System. Journal of Physics: Conference Series 2785 (2024) 012059: 1-12. doi:10.1088/1742-6596/2785/1/012059.
34. Khitrov, A. & Khitrov, A. (2021). Parameters Identification of Induction Motor Drives. In the 28th International Workshop on Electric Drives: Improving Reliability of Electric Drives (IWED), Moscow, Russia. Jan 27 – 29, 2021.
35. Kuznetsov, V., Dmytro, T., & Nikolenko, A. (2024). Identification of Induction Motor Parameters in Vector Control Electric Drives. European Science, 1(sge26-01): 58–103.
36. Bala, A., Adeleke, H. A., Ohemu, M. F., Kyari, I. B. Zubairu, U. I. & Muhammad, B. (2022). Parameters identification of induction motor using bacterial foraging algorithm. International Journal of Engineering and Applied Computer Science (IJEACS), 4(6). 1-11.
37. Bala, A., Adeleke, H. A., Ohemu, M. F., Adamu, T., & Idris, K. (2022). Bacterial Foraging Algorithm Based Parameters Estimation of Induction Motor. IOSR Journal of Electrical and Electronics Engineering (IOSR-JEEE), 17(6). 11-25.
38. Terron-Santiago, C., Martinez-Roman, J., Puche-Panadero, R., & Sapena-Bano, A. (2021). A Review of Techniques Used for Induction Machine Fault Modelling. MPDI Sensors Journal, 21(2021): 1-18. https://doi.org/10.3390/s21144855.
39. Zhao Z., Fan F., Sun Q., Tu P., & See K. Y. (2022). High-Frequency Modeling of Induction Motor Using Multilayer Perceptron. Asia-Pacific International Symposium on Electromagnetic Compatibility (APEMC), 222 - 224. https://doi.org/10.1109/APEMC53576.2022.9888414.
40. Odhano, S. A., Pescetto, P., Awan, H. A. A., Hinkkanen, M., Pellegrino, G., & Bojoi, R. (2019). Parameter Identification and Self-Commissioning in AC Motor Drives: A Technology Status Review. IEEE Transactions on Power Electronics, 34(4): 3603–3614. doi: 10.1109/TPEL.2018.2856589.
41. Wuri, B. H. (2022). The Effect of Motor Parameters on the Induction Motor Speed Sensorless Control System using Luenberger Observer. International Journal of Applied Sciences and Smart Technologies, 4(1): 59–74.